JOURNAL OF GEOPHYSICAL RESEARCH: SOLID EARTH, VOL. 118, 3837–3847, doi:10.1002/jgrb.50265, 2013

Coseismic slip distribution for the M_w 9 2011 Tohoku-Oki earthquake derived from 3-D FE modeling

C. Kyriakopoulos,[1,2] T. Masterlark,[3] S. Stramondo,[2] M. Chini,[4,2] and C. Bignami[2]

Received 25 February 2013; revised 21 June 2013; accepted 23 June 2013; published 30 July 2013.

[1] The coseismic slip distribution of the M_w 9.0 2011 Tohoku-Oki earthquake has been estimated by inverting near-field onshore and offshore geodetic data, using Green's function calculated with a 3-D finite element (FE) model. The FE model simulates several geophysical features of the subduction zone that hosted the rupture surface of the event. These features include a 3-D geometric configuration and distribution of material properties of the tectonic system, a precise geometric configuration of the irregular rupture surface, and an irregular free surface according to the topography and bathymetry. A model that simulates rupture along the interface between the relatively weak overriding Okhotsk plate and stiff subducting slab of the Pacific Plate requires less slip to produce the observed surface deformation, compared to a model having uniform material properties across the rupture interface. Furthermore, the estimated slip of the heterogeneous model is more widely distributed over the shallow portion of the plate boundary, whereas the estimated slip of the homogeneous model is more focused updip of the epicenter. This demonstrates the sensitivity of inverse analyses of geodetic data for the 2011 Tohoku-Oki earthquake to the simulated domain geometry and configuration of material properties.

Citation: Kyriakopoulos, C., T. Masterlark, S. Stramondo, M. Chini, and C. Bignami (2013), Coseismic slip distribution for the M_w 9 2011 Tohoku-Oki earthquake derived from 3-D FE modeling, *J. Geophys. Res. Solid Earth*, *118*, 3837–3847, doi:10.1002/jgrb.50265.

1. Introduction

[2] On 11 March 2011, at 05:46 UTC, a M_w 9.0 (U.S. Geological Survey (USGS)) earthquake struck near the Tohoku region of the northeastern coast of Japan (Figure 1), causing large seafloor displacement that triggered a tsunami. This tsunami caused extensive damage and destruction along the coast of the Tohoku region. This megathrust event, hereafter referred to as the 2011 Tohoku-Oki earthquake, was recorded by a variety of modern geophysical instruments and dense observational networks. The Tohoku-Oki event, the greatest ever recorded in Japan, joins a small group of megathrust events recorded with modern instrumentation including, 1952 Kamchatka (M_w 9.0), 1960 Chile (M_w 9.5), 1964 Alaska (M_w 9.2), and 2004 Sumatra (M_w 9.0) earthquakes (USGS). Data from more than 1200 terrestrial GPS sites (GEONET), managed from the Geospatial Information Authority of Japan were processed by the ARIA team at Jet Propulsion Laboratory (JPL) and Caltech to obtain the 3-D displacement field over Japan and surrounding islands (ftp://sideshow.jpl.nasa.gov/pub/usrs/ARIA). The displacement field shows that the coast of northeast Japan moved 5 m eastward, and the coastline subsided by about 0.5 m with a maximum subsidence of ~1.1 m in the eastern Miyagi Prefecture. For the first time, coseismic displacements from seafloor geodetic sites [*Sato et al.*, 2011] recorded the offshore displacement for a megathrust event, allowing for unprecedented and important offshore geodetic constraints on the source characterization. These observations include large horizontal displacements of ~24 m and vertical displacements of 1.5–3 m, over the hypocentral area. Perhaps most importantly, the offshore geodetic sites precisely define the position of the polarity change for the offshore vertical deformation [*Sato et al.*, 2011], which strongly controls the general depth of the estimated slip.

[3] The coseismic slip distribution of the Tohoku-Oki earthquake has been investigated by numerous authors based on seismological data [e.g., *Ammon et al.*, 2011], onshore/offshore geodetic data [e.g., *Grilli et al.*, 2012; *Pollitz et al.*, 2011], and tsunami data and joint inversions [e.g., *Koketsu et al.*, 2011; *Romano et al.*, 2012; *Simons et al.*, 2011; *Hooper et al.*, 2013]. Several studies have suggested that very large coseismic slip, exceeding 50–60 m, occurred near the Japan Trench [*Linuma et al.*, 2012; *Ito et al.*, 2011a, 2011b; *Lay et al.*, 2011; *Maeda et al.*, 2011; *Shao et al.*, 2011; *Hooper et al.*, 2013], while other studies

Additional supporting information may be found in the online version of this article.

[1]School of Earth and Atmospheric Sciences, Georgia Institute of Technology, Atlanta, Georgia, USA.
[2]National Earthquake Center, Istituto Nazionale di Geofisica e Vulcanologia, Rome, Italy.
[3]Geology and Geological Engineering, South Dakota School of Mines and Technology, Rapid City, South Dakota, USA.
[4]Département Environnement et Agro-biotechnologies (EVA), Centre de Recherché Public - Gabriel Lippmann, Belvaux, Luxembourg.

Corresponding author: C. Kyriakopoulos, School of Earth and Atmospheric Sciences, Georgia Institute of Technology, Ford ES&T Building, 311 Ferst Drive, Atlanta, Georgia 30332-0340, USA. (kyriakopoulos@gatech.edu)

2169-9313/13/10.1002/jgrb.50265

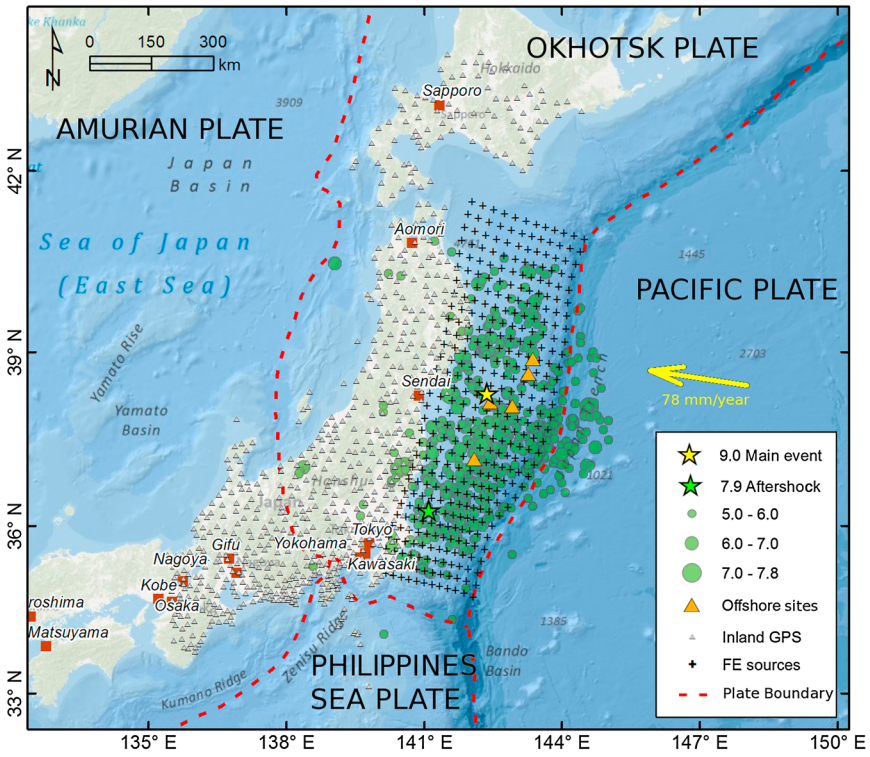

Figure 1. Seismotectonics of the 2011 M_w 9 Tohoku earthquake. Main event and aftershocks spanning 2 months after the 11 March 2011 provided by the National Earthquake Information Center (http://earthquake.usgs.gov/regional/neic/). The aftershocks illuminate the surface projection of the rupture, although some of them spillover onto the Pacific Plate (east of the Japan Trench) in accord with coseismic stress transfer to the extensional region of the main shock [*Lay et al.*, 2009]. The black crosses superimposed on the seismicity show the partitioning of the subducting interface in discrete sources. The yellow and green stars indicate the epicenters of the 2011 Tohoku earthquake and the largest (M_w 7.3) aftershock.

estimate substantially lower peak slips of 30–35 m [*Koketsu et al.*, 2011; *Pollitz et al.*, 2011; *Hayes* [2011]; *Ozawa et al.*, 2011]. These differences are ascribed on the adopted data selection and specific modeling strategies. For example, seismological studies use models that incorporate layered seismic velocity structure for the source estimation, while geodetic models often rely on homogeneous half spaces [e.g., *Okada*, 1992] or layered spherical models [*Pollitz et al.*, 2011]. Furthermore, the estimated maximum coseismic slip value varies from ~20 to ~35 m between inversions with and without the offshore GPS vectors [*Pollitz et al.*, 2011; *Ozawa et al.*, 2011]. The availability of the offshore geodetic observations requires a careful consideration of the subduction interface, which gives us the possibility to explore how features such as material contrasts, irregular slab geometry, and topographic surface control the estimation of slip. Accurate characterization of the offshore deformation is particularly important for tsunami genesis predictions [e.g., *Grilli et al.*, 2012]. The aim of this paper is to identify variations in slip predictions associated with geodetic analyses that use different deformation model configurations. Therefore, we refrain from using tsunami data to constrain the seafloor deformation. This analysis has important implications for emerging methods that attempt to provide early warning for tsunami hazards, based on observed geodetic data [e.g., *Blewitt et al.*, 2006; *Sobolev et al.*, 2007].

2. Finite Element Model

[4] The Tohoku-Oki earthquake ruptured the interface separating the Pacific and Okhotsk Plates. The main event was primarily thrust (gCMT, http://www.globalcmt.org) having substantial slip along the updip portion of the rupture, near the Japan Trench. We simulate the coseismic deformation of the Tohoku-Oki earthquake using FE models, constrained by an array of geophysical data and information. The geometry and mesh of the new FE model presented in this study (Figure 2) is generated with the CUBIT 12.2 geometry and mesh generation tool kit (http://cubit.sandia.gov/index.html), while the material properties, boundary conditions, and loading specifications are part of the input for a finite element analysis (solver) using the ABAQUS commercial code (www.simulia.com). The FE model presented in this paper simulates important geometric and geophysical features of the subduction zone and rupture of the Tohoku-Oki earthquake. These features include the irregular surface of the Japan Trench and subducting Pacific Plate, regional-scale topography and bathymetry (Figure 2b), and an assembly of

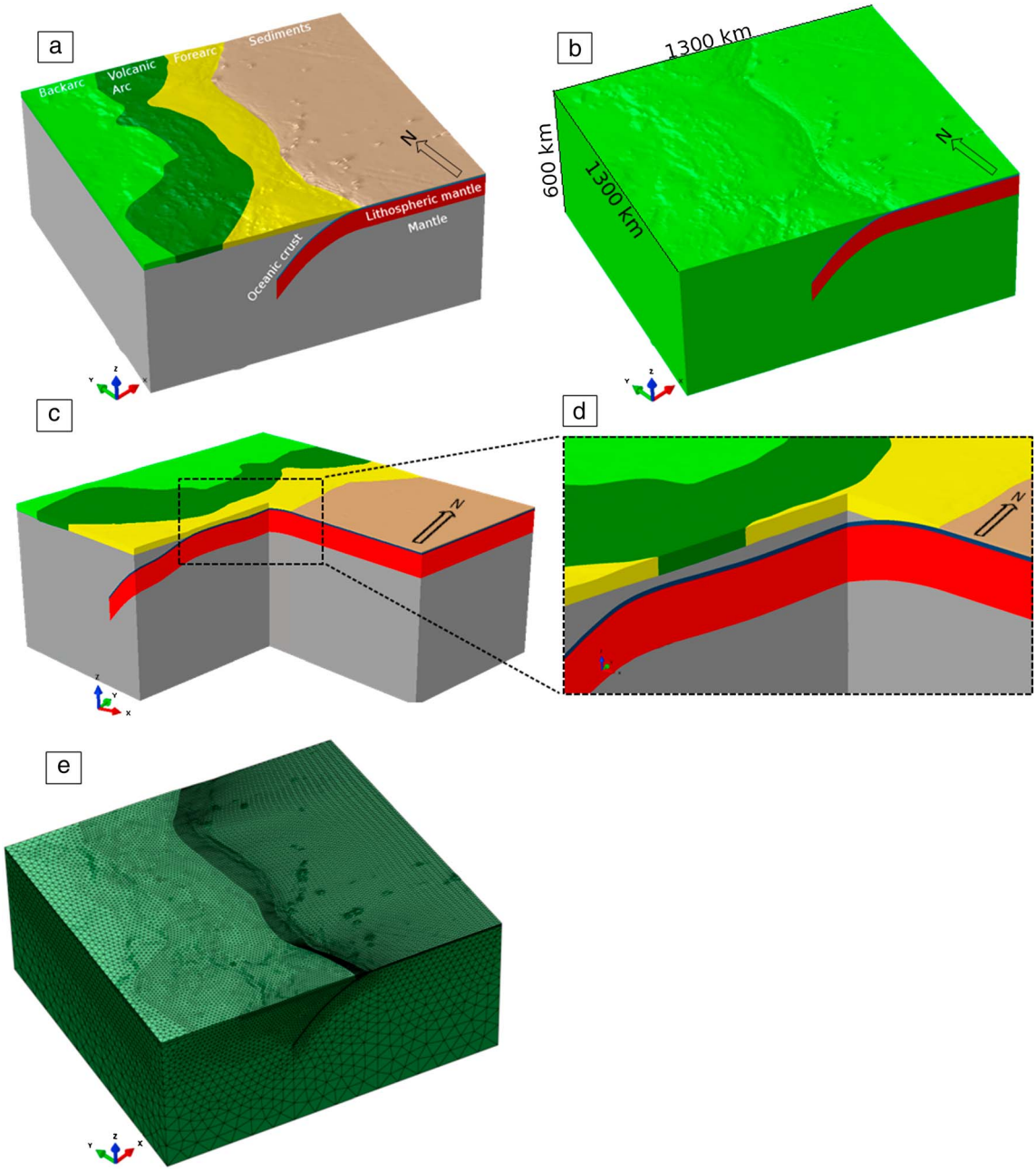

Figure 2. Finite element model configuration. The finite element (FE) model simulates the Honshu Arc subduction zone, Japan. (a) Mechanical components: forearc (yellow), volcanic arc (dark green), backarc (light green), lithosphere (red), crust (blue), mantle (gray). The Young modulus and Poisson ratio values are fixed for each geologic entity. (b) A combination of topography and bathymetry (ETOPO1 project) describes the free surface of the model. The dimensions of the central sector of the model are 1300 km × 1300 km × 600 km. (c, d) 3-D section of the FE model illuminates the rigidity contrasts between the upper crust and the down-going slab. (e) Mesh grid of the model. For visual clarity we hide element edges in (a),(b),(c), and (d). The final model is composed of more than one million first-order tetrahedral elements. The mesh grid density is higher around the simulated rupture interface and progressively coarsens toward the boundaries of the model domain. The average edge sizes for each tetrahedron are ~10 km near the fault area, ~30 km at the lateral boundaries, and ~90 km near the bottom of the model.

the major mechanical components that comprise the subduction zone (Figures 2a, 2c, and 2d).

[5] Topography and bathymetry are modified from the ETOPO1 Global Relief Project (http://www.ngdc.noaa.gov/mgg/global/global.html) and imported into the CUBIT mesh generator software using a python script from GEOCubit [*Casarotti et al*., 2008]. A precise geometric characterization of the subduction interface, and hence the rupture surface, is important because it is fundamental to the deformation pattern of coseismic slip. Therefore, the FE mesh includes an

Table 1. Material Properties

Material	Source	Young Modulus (GPa)	Poisson Ratio
Hanford basalt	*Wang* [2000]	56	0.31
Lithospheric mantle	*Turcotte and Schubert* [2002]	150	0.25
Volcanic arc	*Wang* [2000]	40	0.34
Mantle	*Turcotte and Schubert* [2002]	150	0.25
Backarc sediment (Berea sandstone)	*Wang* [2000]	15	0.34
Backarc basement	*Turcotte and Schubert* [2002]	70	0.28
Forearc (Berea sandstone)	*Wang* [2000]	15	0.34
Sedimentary wedge (Berea sandstone)	*Wang* [2000]	15	0.34
Sediments over crust	*Wang* [2000]	56	0.31

accurate description of the geometrically irregular slab [*Hayes et al*., 2012], giving particular attention to the intersection of the slab and the bathymetric surface of the seafloor. This is important to accurately represent the along-trench subduction morphology and the spatial relationships between the rupture and Earth's free surface—important parameters for accurately assessing the earthquake rupture. The rupture zone in our model occurs along a ~740 km long interface, separating the subducting slab (lithospheric mantle capped by basalt of the oceanic crust) from the overriding forearc and upper mantle wedge. The geometry of the forearc, volcanic arc, and backarc basins is estimated from seismic tomography and the three-dimensional Mohorovicic discontinuity model of *Zhao et al*. [1992]. The resulting FE configurations include a 3-D representation of the major mechanical bodies of the tectonic system (Figure 2 and Table 1), generally represented by other models that do not account for along-strike variations associated with the transition between island arc volcanism and backarc spreading [e.g., *Grilli et al*., 2012]. Material properties for each component are estimated from characteristic selections of elastic [*Turcotte and Schubert*, 2002] and poroelastic [*Wang*, 2000] rock properties. The final model comprises more than one million tetrahedral elements with high element density near the simulated rupture interface and becoming sparse toward the boundaries of the model domain. The characteristic length for elements is ~10 km near the fault area and progressively increases to ~30 km at the lateral boundaries and ~90 km near the bottom boundaries of the model (Figure 2e).

[6] The initial conditions are equilibrium. The lateral boundaries and base of the model domain are fixed to zero displacement. The two converging plates (footwall and hanging wall) are welded together along the nonslipping portions of the plate boundary. The rupture interface is partitioned into 372 coincident node pairs (31×12 fault patches of ~24×20 km size) to allow for a distribution of coseismic slip (calibration parameters), which will be estimated from geodetic data using linear inverse methods. The forward model for deformation due to an assembly of fault patches embedded in an elastostatic domain is

$$\mathbf{G}\,\mathbf{m} = \mathbf{d} \tag{1}$$

where **G** is a matrix of Green's function, **m** is a column vector of slip parameters, and **d** is a column vector of data. For this analysis, **G** is constructed using FEs and the method of kinematic constraint equations [*Masterlark*, 2003] and implemented with the configuration of *Kyriakopoulos et al*. [2011]. The vector **m** represents the unknown distribution of slip for the fault patches (vector of calibration parameters), and **d** (vector of calibration targets) is constructed from a dense array of onshore GPS solutions (708 sites) released by the ARIA JPL-Caltech team (ftp://sideshow.jpl.nasa.gov/pub/usrs/ARIA) and five three-component seafloor displacement observations collected using GPS/acoustic methods [*Sato et al*., 2011].

[7] The inversion is performed adopting the Occam regularization scheme [*deGroot-Hedlin and Constable*, 1990], minimizing the chi-square and an additional roughening term to avoid unreasonable oscillations in slip values. The roughening term represents the square of the finite difference operator between adjacent patches, multiplied by a weighting factor k. No positivity constraints are used in this inversion. The misfit vector, **e**, is

$$\mathbf{e} = \mathbf{d} - \mathbf{G}\,\mathbf{m}^{\text{est}} \tag{2}$$

where $\mathbf{m}^{\text{est}}$ is the estimate of **m** based on the Occam method.

[8] The onshore and offshore data have significant differences in terms of dimensions and measurement uncertainties. The average uncertainty for the onshore GPS observations is ~3.2 cm, while the corresponding uncertainty for the offshore sites is greater by a factor of 10 (~33 cm). The data vector **d** used in the linear inversion is a column vector having 2139 elements, assembled from 2124 ($= 708 \times 3$) onshore and 15 ($= 5 \times 3$) offshore components. The data are weighted according to the reported measurement uncertainties, and the offshore sites are additionally weighted by 10.

[9] The estimated fault slip distribution is selected from a chi-square (χ^2)-roughness (ρ) trade-off analysis [*Jónsson et al*., 2002], where diminishing reductions in chi-square prediction errors require accelerated increases in solution roughness (see Figures S1 and S2 in the supporting information). As expected, the rougher solutions are more accurate, achieving a root-mean-square (RMS) of 2 and 3 cm for the homogeneous (JHOT) and heterogeneous (JHET) models, respectively (see Figures S3–S6). In order to compare the slip maps generated from JHET and JHOT, we have chosen two statistically equivalent solutions, coincident with the intersection of the JHET and JHOT chi-square (χ^2)-roughness (ρ) curves. This statistical equivalence is established using statistical hypothesis testing methods and F tests, as described in [*Masterlark et al*., 2012]. These methods indicate that both JHET and JHOT well fit the data and are statistically similar, with 95% confidence. These results are summarized in Table 2.

Table 2. F Test[a]

	d.f.	$\mathbf{e}^{\mathrm{T}}\mathbf{e}$	σ^{est}	χ^2	$F_{\text{critical}}(95\%)$	F
Null	2,139	-	-	2,915,914.9	-	-
JHET	2,099	10.7	0.071	9,120.9	-	-
JHOM	2,104	14.9	0.084	9,671.8	-	-
			Comparisons			
Null/JHET	-	-	-	-	1.074	313.659
Null/JHOM	-	-	-	-	1.074	296.535
JHOM/JHET	-	-	-	-	1.074	1.0577

[a] $N = 2139$ for all analyses.

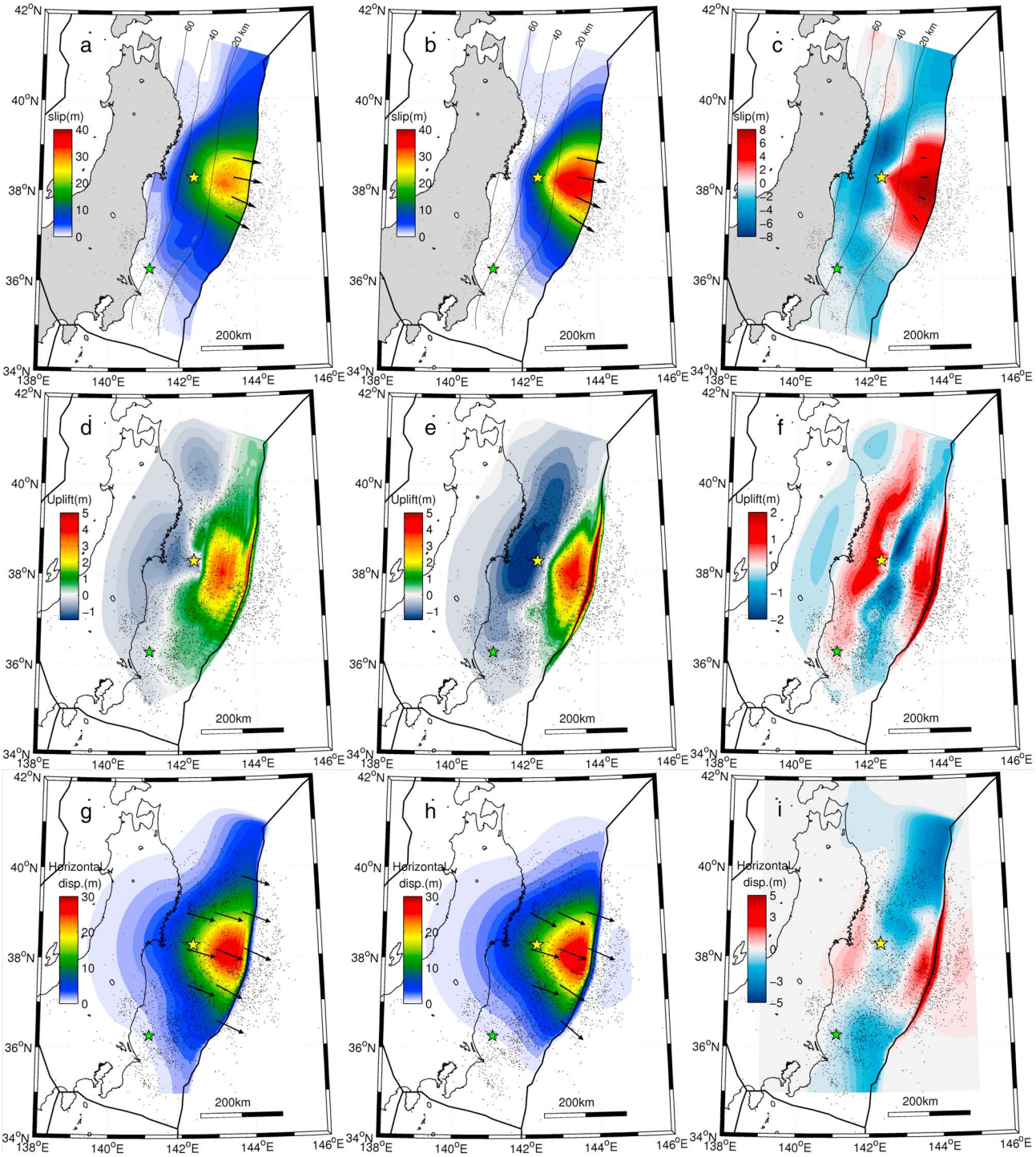

Figure 3. Coseismic slip and surface displacement. (a, b) Slip distribution for the heterogeneous (JHET) model and the homogeneous (JHOT) model, respectively. (c) Differences between JHOT and JHET models (Diff = JHOT – JHET). (d) Seafloor uplift for JHET model. (e) Seafloor uplift for JHOT model. (f) Differences in seafloor uplift between JHOT and JHET models (Diff = JHOT – JHET). (g) Seafloor horizontal displacement for JHET model. (h) Seafloor horizontal displacement for JHOT model. (i) Differences in horizontal displacement between JHOT and JHET models (Diff = JHOT – JHET). The black arrows in Figures 3a and 3b represent selected rake vectors for each model while the black vectors in Figures 3g and 3h show the direction of horizontal displacement. The black thin line in (a), (b) and (c) shows depth contours for the modeled subduction interface. The yellow and green stars indicate the epicenters of the 2011 Tohoku earthquake and the largest (M_w 7.3) aftershock.

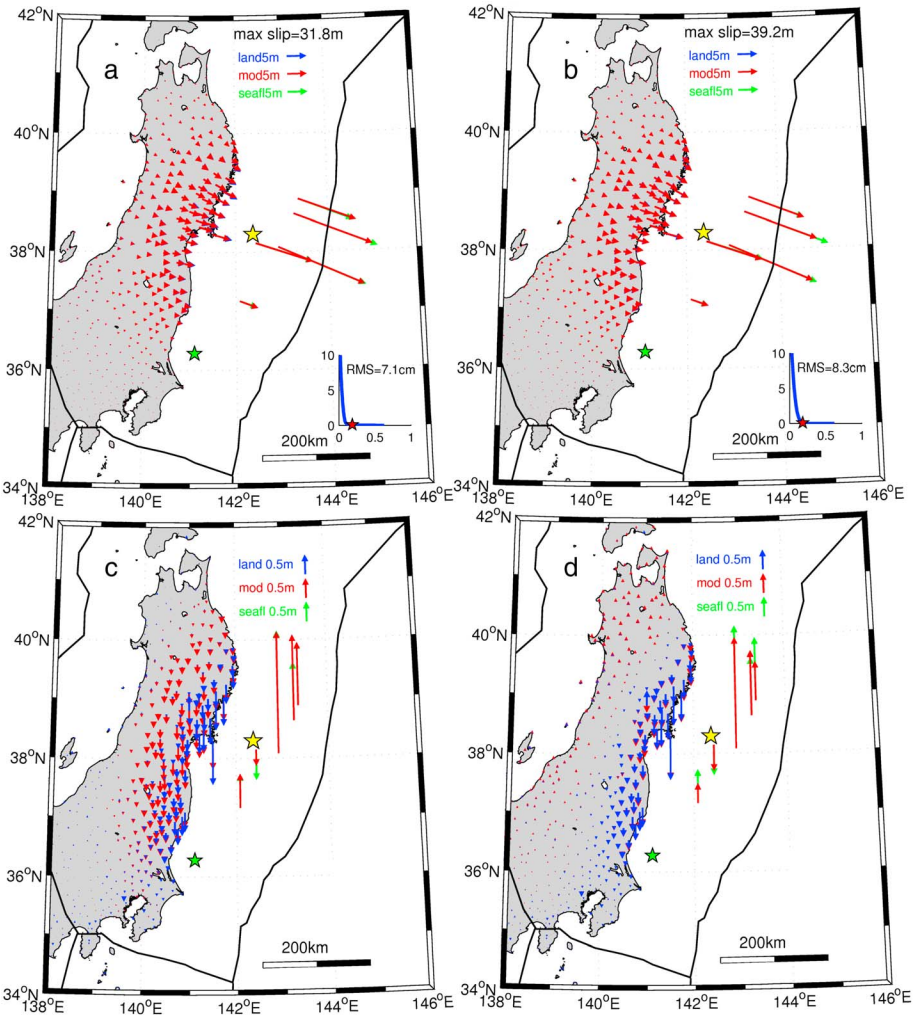

Figure 4. Comparison between predicted and observed GPS data. (a) Horizontal JHET model predictions. (b) Horizontal JHOT model predictions. (c) Vertical JHET model predictions. (d) Vertical JHOT model predictions. Modeled GPS vectors (red), seafloor GPS observations (green), onshore GPS observations (blue). The yellow and green stars indicate the epicenters of the 2011 Tohoku earthquake and the largest (M_w 7.3) aftershock. The inset at the bottom right corner in (a) and (b) shows the X^2 (y axis)-ρ (roughness) (x axis) curve and a red star denoting our selected solution with relative root-mean-square (RMS). See also Figures S3–S6.

[10] The resulting slip distribution for JHET is shown in Figure 3a and is equivalent to a geodetic moment of 2.03×10^{22} N m, corresponding to M_w 8.8, slightly lower with respect to previous studies. This value is lower than the accepted M_w 9.0 because the moment estimation for JHET is proportional to local material selection, and specifically the low shear modulus values near the shallow dipping sector of the subducting slab. The slip distribution is concentrated directly updip of the earthquake hypocenter and close to the trench, but includes deeper and lateral components of the slip as well. The model predictions of the horizontal and vertical GPS data are shown in Figure 4. The area of rupture exceeding 15 m is ~200×140 km^2, while the maximum slip value is ~32 m. The high-slip region partially coincides with the location of high seismic coupling inferred from interseismic crustal velocity measurements [*Hashimoto et al*., 2009; *Loveless and Meade*, 2010], but it is generally well updip of the highly coupled area inferred in these studies, because of the use of the offshore geodetic data in the linear inversion.

[11] The distinct role played by onshore and offshore geodetic observations has been exploited in previous works [*Pollitz et al*., 2011]. Even if onshore geodetic observations successfully describe the inland deformation, they typically have poor sensitivity to the offshore slip [e.g., *Masterlark*, 2003]. We overcome this limitation by using offshore geodetic observations that help us discriminate between the deeper and shallower components of the slip. By comparing Figures 5a and 3a which use only inland and all data, respectively, we see that slip inversions which do not account for the offshore geodetic sites tend to localize the displacement at greater depth along the interplate boundary and thus cannot adequately discriminate relatively deep slip from shallow slip. Furthermore, we conducted a checkerboard test to estimate the contribution of onshore and offshore geodetic sites on the resolution of estimated slip values (Figure 6). We

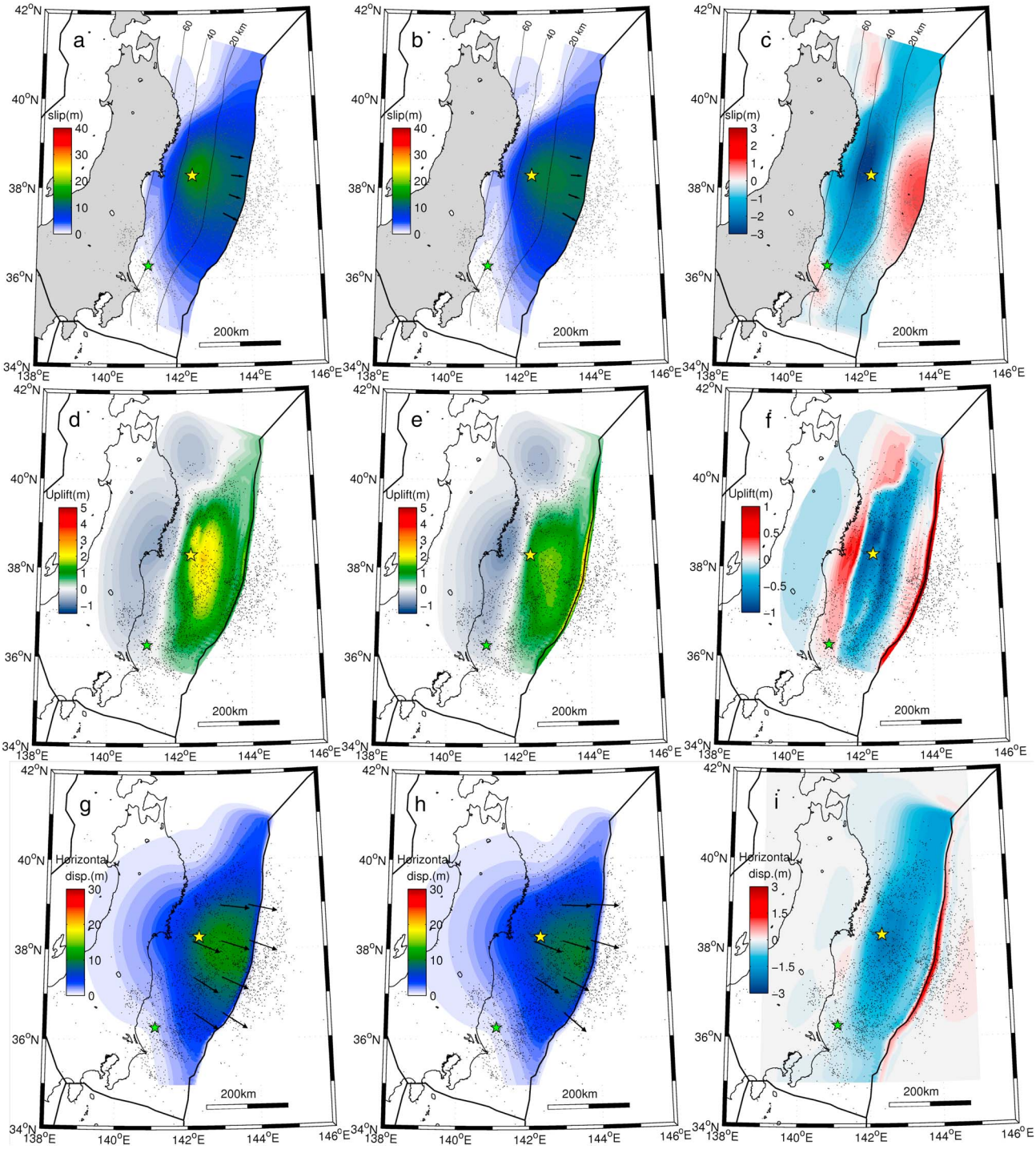

Figure 5. Coseismic slip distribution and surface displacement using only inland GPS sites. (a, b) Slip distribution for the heterogeneous (JHET) model and homogeneous (JHOT) model, respectively. (c) Differences between JHOT and JHET models (Diff = JHOT – JHET). (d) Seafloor uplift for JHET model. (e) Seafloor uplift for JHOT model. (f) Differences in seafloor uplift between JHOT and JHET models (Diff = JHOT – JHET). (g) Seafloor horizontal displacement for JHET model. (h) Seafloor horizontal displacement for JHOT model. (i) Differences in horizontal displacement between JHOT and JHET models (Diff = JHOT – JHET). The black arrows in Figures 5a and 5b represent selected rake vectors for each model while the black vectors in Figures 5g and 5h show the direction of horizontal displacement. The black thin line in (a), (b) and (c) shows depth contours for the modeled subduction interface The yellow and green stars indicate the epicenters of the 2011 Tohoku earthquake and the largest (M_w 7.3) aftershock.

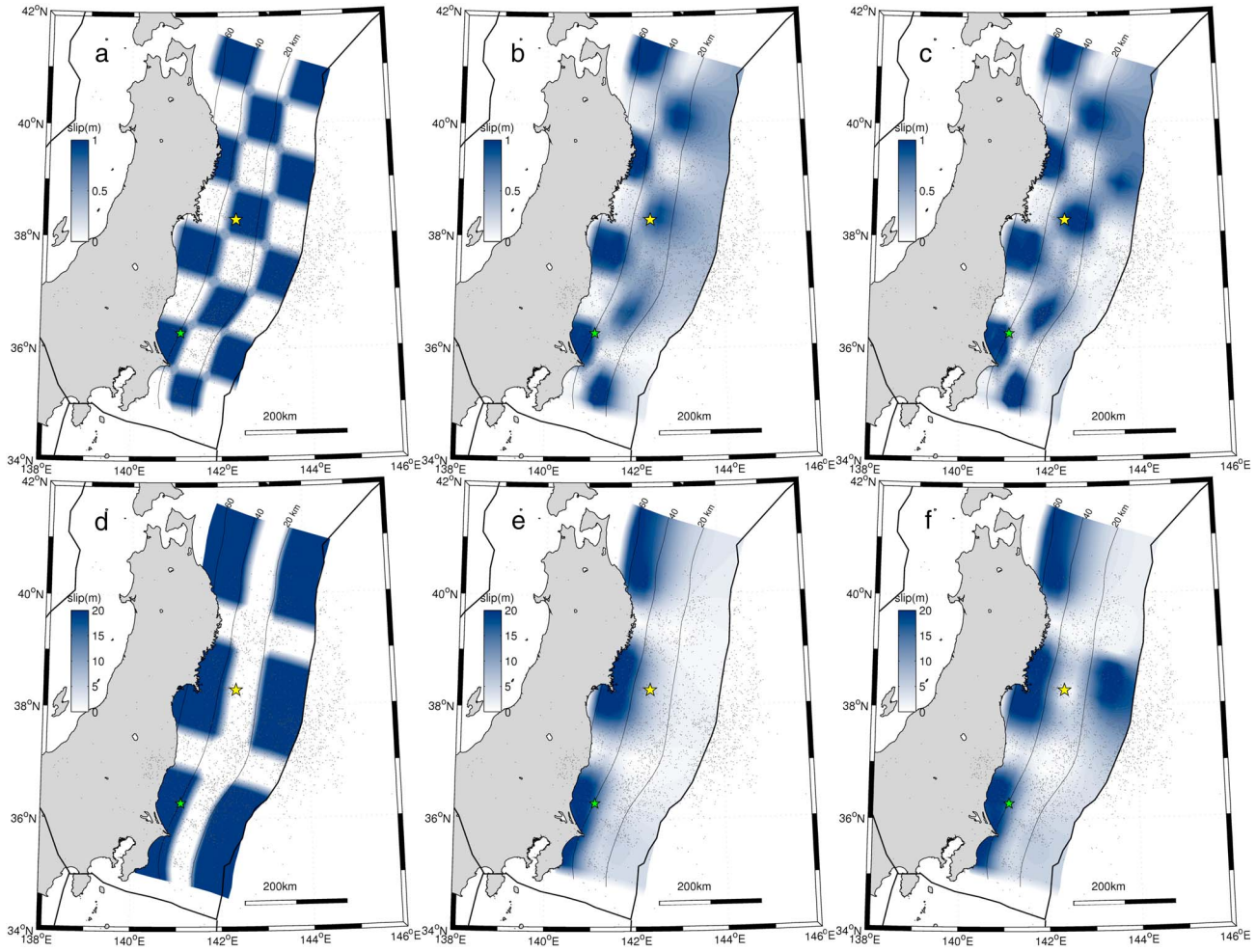

Figure 6. Resolution test. (a) Input slip model (4 × 4 groups of patches with 0 and 1 m of slip) used for the checkerboard test. (b) Results of the checkerboard test for inversion of the onshore GPS data. (c) Results of the checkerboard test for joint inversion of onshore GPS + offshore geodetic coseismic data. (d) Input slip model (8 × 4 groups of patches with 0 and 20 m of slip). (e) Results for inversion of the onshore GPS data. (f) Results for joint inversion of onshore GPS + offshore geodetic coseismic data.

are using two different checkerboard inputs. The first one (Figure 6a) consists of a finer pattern (4 × 4 groups of patches) and lower slip values (0 and 1 m) while the second one (Figure 6d) investigates larger asperities (8 × 4 groups of patches) and higher slip values (0 and 20 m). When only onshore GPS data are used for the resolution test inversion (Figures 6b and 6e), lateral variations in the slip are well resolved only below the 20 km depth contour line. The addition of seafloor geodetic data increases the resolution above the 20 km depth contour line, mostly in the central and northern sectors of our fault model, where part of the shallow displacement occurs (Figures 6c and 6f). Figure 6f demonstrates the importance of offshore geodetic data for characterizing near-trench seafloor deformation that can strongly influence tsunami genesis.

[12] The effect of material inhomogeneities is presented in Figure 3 by comparing the slip distributions of the JHET model versus the homogeneous counterpart (JHOT) and plotting the differences between the two. The JHOT slip distribution is presented in Figure 3b. The estimated geodetic moment is 4.57×10^{22} N m which corresponds to M_w 9.04 (using an average rigidity of 40 GPa) and larger than that of JHET. We note that for the case of homogeneous material properties, the estimated slip distribution is a function of Poisson's ratio and is independent of rigidity.

[13] From a first look, we can notice that both models predict a high concentration of slip above 20 km depth and toward the surface. Furthermore, the JHET slip is distributed in a much larger area, extending farther north with respect to the JHOT slip, which is concentrated closer to the trench. In contrast, the JHET model predicts lower slip values near the trench and higher slip farther downdip, close to the hypocenter. Differences of up to 25% are highlighted from the red (JHOT > JHET) and blue (JHET > JHOT) areas in Figure 3c, coincident with the transition of contact from oceanic crust/forearc to oceanic crust/mantle. The same transition marks an inversion in terms of relative stiffness between hanging wall and footwall, and the oceanic crust is stiffer in respect to the forearc but less stiff in respect to the mantle. The two models present substantially different results

in terms of maximum slip values, with ~32 and 39 m for JHET and JHOT, respectively. Indeed, the weak crustal materials (i.e., contrast between oceanic crust and forearc) implemented in the heterogeneous model amplifies the surface displacement for a given dislocation. This effect is manifested in the matrix of Green's function, calculated using JHET; hence, the JHET model requires a smaller amount of slip in order to fit the data.

[14] These results follow the findings of *Hsu et al*. [2011] for the Sumatra subduction zone, where discrepancies between homogeneous and heterogeneous models become larger if the elastic contrast between the two sides of the fault is increased. Using FE-based inverse methods, *Masterlark et al*. [2001] noted that for a given array of surface displacements, a heterogeneous model requires less coseismic slip compared to a homogeneous model. These differences increase with increasing rigidity contrasts across the fault [*Hsu et al*., 2011]. Slip variations due to rigidity contrasts are also found in *Trasatti et al*. [2011] where the implementation of a high-resolution seismic tomography in the FE model significantly affects the slip distribution pattern.

[15] Our results become intuitive by considering the limiting case, in which the subducting slab is infinitely stiff compared to the overriding plate. In this case the relative slip is accommodated almost entirely by the overriding plate, whereas in the homogeneous half-space configuration the overriding plate receives only half of the relative slip. In the shallow part of the fault, the rigidity contrast between forearc and subducting crust enhances the asymmetry produced by the free surface effect. This explains why the maximum slip value of JHET is less than that of JHOT especially in our case where the solutions are constrained by the offshore coseismic data.

[16] Even though in a reduced degree, differences between JHET and JHOT models remain for slip inversions that do not account for the offshore geodetic data (Figure 5). Similar to the full data set case, the JHET predicts higher slip values downdip and lower slip values near the trench with respect to JHOT (Figure 5c). The results are different in terms of maximum slip values with 15 and 13.5 m for JHET and JHOT, respectively, highlighting the impact of the offshore data on the retrieved solutions. The slip is concentrated downdip in the fault plane, where the rigidity contrast is inverted with respect to the shallower part of the fault. In this case the hanging wall (mantle) is stiffer compared to the footwall (oceanic crust). The slip differences between the two models are lower and corresponding to 10–20% of maximum slip values (Figure 5c). The estimated geodetic moment is 3.13×10^{22} N m, corresponding to M_w 8.94 (using an average rigidity of 40 GPa), for JHOT and 1.74×10^{22} N m, corresponding to M_w 8.77, for JHET.

[17] The predicted surface displacement maps generated by JHET and JHOT models are presented in Figures 3d–3i (joint inversion of inland GPS + offshore geodetic sites). As expected, the vertical (uplift) and horizontal displacements reflect the differences in slip pattern. The uplift predicted from JHET (Figure 3d) is less concentrated compared to that from JHOT (Figure 3e) and distributed in a much larger area. The maximum uplift value predicted from JHET is 4 m while that from JHOT is more than 7.5 m and close to the trench (note color saturation in Figure 3e), as result of the intersection of the slip patch with the seafloor. The predicted horizontal displacement for JHET (Figure 3g) is widely distributed compared to that for JHOT (Figure 3h), reaching maximum values of 28 and 29 m, respectively. The differences are highlighted from the red (JHOT > JHET) and blue (JHET > JHOT) areas in Figures 3f and 3i. These forward models show clearly the material's effect on the predicted surface displacements. Although the input for each model is substantially different in terms of absolute slip values, the generated horizontal displacement fields present similar magnitudes. The seafloor surface displacement predictions are also plotted for the inversions that do not account for the offshore geodetic data (Figures 5d–5i). We note that without offshore data in our inversion the predicted uplift is higher for JHET. The differences in horizontal and vertical displacement predictions are presented in Figures 5f and 5i.

[18] Recent works, which mapped the changes in the seafloor topography caused by the M_w 9 event [*Kodaira et al*., 2012; *Fujiwara et al*., 2011], revealed that the seafloor moved 50 m east-southeast toward the trench and uplifted 5–10 m . Although the bathymetric data provide new information, they are limited by the lateral extension (10 km width) of the observation track. Furthermore, *Ito et al*. [2011b] reported large coseismic displacements from two clusters of ocean bottom instruments at about 20 (CL1) and 30 km (CL2) from the trench. They measured 58 ± 20 and 74 ± 20 m of horizontal displacement for CL1 and CL2, respectively. These observations are in good agreement with high slip values (73–81 m) obtained from Hooper *et al*. [2013] and constrained from both tsunami and geodetic data. The comparison of our results with observations based on differential bathymetry is not an easy task. Our results appear to be below the lower end of the above values. Our models are not constrained by the tsunami data, which will increase our maximum slip values to 45–55 m, but probably not to 70–80 m of the slip. However, as suggested by *Kodaira et al*. [2012], it is probable that the results based on bathymetric studies include effects beyond the pure elastostatic deformation scenario, such as massive seafloor landslides, slumping, and gravity effects.

[19] Both models adequately recover the horizontal and vertical GPS displacements (Figure 4), even though the JHOT model vertical predictions appear to be slightly more accurate near the east coast of Japan. The small difference in the vertical component for JHET might imply that the elastic parameters we chose need to be calibrated specifically for the Japan Trench.

[20] Slip distribution models based on seismic waveform analysis [*Lay et al*., 2011; *Shao et al*., 2011], waveforms + high rate GPS [*Ammon et al*., 2011] measurements, or the combination of GPS and tsunami data [*Romano et al*., 2012] revealed maximum slip values updip from the hypocenter up to 45–60 m, larger than the maximum values from JHET (~32 m) and JHOT (~40 m) models. On the other hand, our maximum slip values are more comparable with those of *Pollitz et al*. [2011] (30–35 m), which used the same data (onshore GPS + offshore GPS/acoustic). Moreover, similar peak slip values are found by *Hayes* [2011] (~31 m), derived from teleseismic waves, and *Koketsu et al*. [2011] (30–40 m) who conducted separate and joint inversions of different types of data. We suggest that part of the differences between our JHET model and previous studies are ascribed to the influence of the 3-D material properties and more specifically

to the elastic contrast between the subducting crust and surrounding materials. Furthermore, a portion of these differences may also be due to the adopted subduction zone geometry and to the intersection of seafloor topography with the subducting interface, overcoming the rectangular source approximation and flat free surface used in previous studies. Previous studies demonstrated the impact of the Earth's free surface [*Oglesby et al*., 2000] on the relative displacement between footwall and hanging wall in shallow thrust earthquakes, and thus, we expect this to be important in the shallow dipping sector of the subducting slab.

3. Conclusions

[21] We constructed a geodetic finite element model that provides a detailed representation of the Tohoku-Oki earthquake. The coseismic slip was calibrated to onshore and offshore geodetic data, the latter of which provides particularly important constraints. The results for the heterogeneous and homogeneous models highlight the effect of the adopted material properties, which introduce respective slip variations of up to 25%. When we do not constrain the inversion with the offshore geodetic data, the differences between JHET and JHOT are reduced. Our results illuminate the asymmetric slip across a fault that separates materials with contrasting elastic properties. We see that the JHOT model requires 39 m of slip to reproduce the observed 24 m of maximum seafloor horizontal displacement, whereas the JHET model demands only 32 m of slip. Both models account for the same geometry and free surface effect as the simulated fault nears the Japan Trench. Additionally, the JHET model accounts for rigidity contrast between forearc and oceanic crust, increasing the absolute displacement of the hanging wall with respect to the footwall at shallow depths. Thus, the asymmetric partitioning of the slip between the footwall and hanging wall is important for the static displacement predictions and requires further investigation in the future. Furthermore, the availability of offshore geodetic data strongly influences the predicted seafloor deformation near the trench. These results are particularly important for future analyses that seek to characterize tsunami behavior from geodetically based seafloor deformation predictions.

[22] **Acknowledgments.** Support for C.K. was provided through NSF-0847382 to Andrew V. Newman (Postdoc Advisor). This work is supported in part by NSF EAR 0911466 and 1264288 (T.M.). The material is also based upon a work supported by NASA ROSES-Earth Surface and Interior under Jet Propulsion Laboratory (JPL) subcontract 1468758 (T.M.). Academic licensing for ABAQUS was provided by Dassault Systemes Simulia Corp. The authors would like to thank the TERRAFIRMA European Space Agency (ESA) project for partially funding the research activities of C.K. Insightful reviews by Tom Parsons (Editor), the Associate Editor, Andy Hooper, and an anonymous reviewer greatly improved this paper.

References

Ammon, C. J., T. Lay, H. Kanamori, and M. Cleveland (2011), A rupture model of the 2011 off the Pacific coast of Tohoku earthquake, *Earth Planets Space*, *63*(7), 693–696.

Blewitt, G., C. Kreemer, W. C. Hammond, H.-P. Plag, S. Stein and, E. Okal (2006), Rapid determination of earthquake magnitude using GPS for tsunami warning systems, *Geophys. Res. Lett.*, *33*, L11309, doi:10.1029/2006GL026145.

Casarotti, E., M. Stupazzini, S. Lee, D. Komatitsch, A. Piersanti, and J. Tromp (2008), CUBIT and seismic wave propagation based upon the spectral-element method: An advanced unstructured mesher for complex 3D geological media, in *Proceedings of the 16th International Meshing Roundtable*, pp. 579–598, Springer-Verlag.

deGroot-Hedlin, C., and S. Constable (1990), Occam's inversion to generate smooth, two dimensional models from magnetotelluric data, *Geophysics*, *55*(12), 1613–1624, doi:10.1190/1.1442813.

Fujiwara, T., S. Kodaira, T. No, Y. Kaiho, N. Takahashi, and Y. Kaneda (2011), The 2011 Tohoku-Oki earthquake: Displacement reaching the trench axis, *Science*, *334*, 1240.

Grilli, S. T., J. C. Harris, T. S. Tajalli Bakhsh, T. L. Masterlark, C. Kyriakopoulos, J. T. Kirby, and F. Shi (2012), Numerical simulation of the 2011 Tohoku tsunami based on a new transient FEM co-seismic source: Comparison to far- and near-field observations, *Pure Appl. Geophys.*, doi:10.1007/s00024-012-0528-y.

Hashimoto, C., A. Noda, T. Sagiya, and M. Matsu'ura (2009), Interplate seismogenic zones along the Kuril-Japan trench inferred from GPS data inversion, *Nat. Geosci.*, *2*, 141–144.

Hayes, G. P. (2011), Rapid source characterization of the 03-11-2011 Mw 9.0 off the Pacific coast of Tohoku earthquake, *Earth Planets Space*, *63*, 529–534.

Hayes, G. P., D. J. Wald, and R. L. Johnson (2012), Slab1.0: A three-dimensional model of global subduction zone geometries, *J. Geophys. Res.*, *117*, B01302, doi:10.1029/2011JB008524.

Hooper, A., J. Pietrzak, W. Simons, H. Cui, R. Riva, M. Naeije, A. Terwisscha van Scheltinga, E. Schrama, G. Stelling, and A. Socquet (2013), Importance of horizontal seafloor motion on tsunami height for the 2011 Mw=9.0 Tohoku-Oki earthquake, *Earth Planet. Sci. Lett.*, *361*, 469–479, doi:10.1016/j.epsl.2012.11.013.

Hsu, Y.-J., M. Simons, C. Williams, and E. Casarotti (2011), Three-dimensional FEM derived elastic Green's functions for the coseismic deformation of the 2005 M_w 8.7 Nias-Simeulue, Sumatra earthquake, *Geochem. Geophys. Geosyst.*, *12*, Q07013, doi:10.1029/2011GC003553.

Iinuma, T., M. Ohzono, Y. Ohta, and S. Miura (2012), Coseismic slip distribution of the 2011 off the Pacific coast of Tohoku earthquake (M9.0) estimated based on GPS data—Was the asperity in Miyagi-oki ruptured?, *Earth Planets Space*, *63*, 643–648.

Ito, T., K. Ozawa, T. Watanabe, and T. Sagiya (2011a), Slip distribution of the 2011 off the Pacific coast of Tohoku earthquake inferred from geodetic data, *Earth Planets Space*, *63*(7), 627–630.

Ito Y., T. Tsuji, Y. Osada, M. Kido, D. Inazu, Y. Hayashi, H. Tsushima, R. Hino, and H. Fujimoto (2011b), Frontal wedge deformation near the source region of the 2011 Tohoku-Oki earthquake, *Geophys. Res. Lett.*, *38*, L00G05, doi:10.1029/2011GL048355.

Jónsson, S., H. Zebker, P. Segall, and F. Amelung (2002), Fault slip distribution of the 1999 M_w 7.1 Hector Mine, California, earthquake, estimated from satellite radar and GPS measurements, *Bull. Seismol. Soc. Am.*, *92*, 1377–1389.

Kodaira, S., T. No, Y. Nakamura, T. Fujiwara, Y. Kaiho, S. Miura, N. Takahashi, Y. Kaneda, and A. Taira (2012), Coseismic fault rupture at the trench axis during the 2011 Tohoku-Oki earthquake, *Nat. Geosci.*, *5*, 646–650, doi:10.1038/ngeo1547.

Koketsu, K. et al. (2011), A unified source model for the 2011 Tohoku earthquake, *Earth Planet. Sci. Lett.*, *310*(3–4), 480–487.

Kyriakopoulos, C., S. Stramondo, M. Chini, C. Bignami, T. Masterlark, S. Borgstrom, F. Guglielmino, G. Puglisi, and V. Siniscalchi (2011), The 11 March 2011 Tohoku-Oki (Japan) megathrust event: FEM models of coseismic and postseismic deformation captured by DInSAR and GPS data, *Am. Geophys. Union - Fall Meet.*, *2011*, U51B–0040.

Lay, T., H. Kanamori, C. J. Ammon, A. R. Hutko, K. Furlong, and L. Rivera (2009), The 2006-2007 Kuril Islands great earthquake sequence, *J. Geophys. Res.*, *114*, B113208, doi:10.1029/2008JB006280.

Lay, T., C. J. Ammon, H. Kanamori, L. Xue, and M. J. Kim (2011), Possible large near-trench slip during the great 2011 Tohoku (Mw 9.0) earthquake, *Earth Planets Space*, *63*, 687–692.

Loveless, J. P., and B. J. Meade (2010), Geodetic imaging of plate motions, slip rates, and partitioning of deformation in Japan, *J. Geophys. Res.*, *115*, B02410, doi:10.1029/2008JB006248.

Maeda, T., T. Furumura, S. Sakai, and M. Shinohara (2011), Significant tsunami observed at the ocean-bottom pressure gauges during the 2011 off the Pacific coast of Tohoku earthquake, *Earth Planets Space*, *63*(7), 803–808.

Masterlark, T. (2003), Finite element model predictions of static deformation from dislocation sources in a subduction zone: Sensitivities to homogeneous, isotropic, Poisson-solid, and half-space assumptions, *J. Geophys. Res.*, *108*(B11), 2540, doi:10.1029/2002JB002296.

Masterlark, T., C. DeMets, H. F. Wang, J. Stock, and O. Sanchez (2001), Homogeneous vs. heterogeneous subduction zone models: Coseismic and postseismic deformation, *Geophys. Res. Lett.*, *28*(21), 4047–4050.

Masterlark, T., K. L. Feigl, M. Haney, J. Stone, C. Thurber, and E. Ronchin (2012), Nonlinear estimation of geometric parameters in

FEMs of volcano deformation: Integrating tomography models and geodetic data for Okmok volcano, Alaska, *J. Geophys. Res.*, *117*, B02407, doi:10.1029/2011JB008811.

Oglesby, D. D., R. J. Archuleta, and S. B. Nielsen (2000), The dynamics of dip-slip faulting: Explorations in two dimensions, *J. Geophys. Res.*, *105*(B6), 13,643–13,653.

Okada, Y. (1992), Internal deformation due to shear and tensile faults in a half-space, *Bull. Seismol. Soc. Am.*, *82*, 1018–1040.

Ozawa, S., T. Nishimura, H. Suito, T. Kobayashi, M. Tobita, and T. Imakiire (2011), Coseismic and postseismic slip of the 2011 magnitude-9 Tohoku-Oki earthquake, *Nature*, *475*, 373–376.

Pollitz, F. F., R. Bürgmann, and P. Banerjee (2011), Geodetic slip model of the 2011 M9.0 Tohoku earthquake, *Geophys. Res. Lett.*, *38*, L00G08, doi:10.1029/2011GL048632.

Romano, F., A. Piatanesi, S. Lorito, N. D'Agostino, K. Hirata, S. Atzori, Y. Yamazaki, and M. Cocco (2012), Clues from joint inversion of tsunami and geodetic data of the 2011 Tohoku-Oki earthquake, *Sci. Rep.*, *2*, 385.

Sato, M., T. Ishikawa, N. Ujihara, S. Yoshida, M. Fujita, M. Mochizuki, and A. Asada (2011), Displacement above the hypocenter of the 2011 Tohoku-Oki earthquake, *Science*, *332*(6036), 1395.

Simons, M. et al. (2011), The 2011 magnitude 9.0, Tohoku-Oki earthquake: Mosaicking the megathrust from seconds to centuries, *Science*, *332*(6036), 1421–1425.

Shao, G., X. Li, C. Ji, and T. Maeda (2011), Focal mechanism and slip history of 2011 Mw 9.1 off the Pacific coast of Tohoku earthquake, constrained with teleseismic body and surface waves, *Earth Planets Space*, *63*(7), 559–564.

Sobolev, S. V., A. Y. Babeyko, R. Wang, A. Hoechner, R. Galas, M. Rothacher, D. V. Sein, J. Schröter, J. Lauterjung, and C. Subarya (2007), Tsunami early warning using GPS-Shield arrays, *J. Geophys. Res.*, *112*, B08415, doi:10.1029/2006JB004640.

Trasatti, E., C. Kyriakopoulos, and M. Chini (2011), Finite element inversion of DInSAR data from the Mw 6.3 L'Aquila earthquake, 2009 (Italy), *Geophys. Res. Lett.*, *38*, L08306, doi:10.1029/2011GL046714.

Turcotte, D. L., and G. J. Schubert (2002), *Geodynamics: Applications of Continuum Physics to Geological Problems*, 2nd ed., 456 pp., Cambridge Univ. Press, New York.

Wang, H. F. (2000), *Theory of Linear Poroelasticity: With Applications to Geomechanics and Hydrogeology*, Princeton Univ. Press, Princeton, N. J.

Zhao, D., A. Hasegawa, and S. Horiuchi (1992), Tomographic imaging of P and S wave velocity structure beneath northeastern Japan, *J. Geophys. Res.*, *97*(B13), 19,909–19,928.